

Inkjet-Printed Micrometer-Thick Perovskite Solar Cells with Large Columnar Grains

Helge Eggers,* Fabian Schackmar,* Tobias Abzieher, Qing Sun, Uli Lemmer, Yana Vaynzof, Bryce S. Richards, Gerardo Hernandez-Sosa, and Ulrich W. Paetzold*

Transferring the high power conversion efficiencies (PCEs) of spin-coated perovskite solar cells (PSCs) on the laboratory scale to large-area photovoltaic modules requires a significant advance in scalable fabrication methods. Digital inkjet printing promises scalable, material, and cost-efficient deposition of perovskite thin films on a wide range of substrates and in arbitrary shapes. In this work, high-quality inkjet-printed triple-cation (methylammonium, formamidinium, and cesium) perovskite layers with exceptional thicknesses of $>1 \mu\text{m}$ are demonstrated, enabling unprecedentedly high PCEs $> 21\%$ and stabilized power output efficiencies $> 18\%$ for inkjet-printed PSCs. In-depth characterization shows that the thick inkjet-printed perovskite thin films deposited using the process developed herein exhibit a columnar crystal structure, free of horizontal grain boundaries, which extend over the entire thickness. A thin film thickness of around $1.5 \mu\text{m}$ is determined as optimal for PSC for this process. Up to this layer thickness X-ray photoemission spectroscopy analysis confirms the expected stoichiometric perovskite composition at the surface and shows strong deviations and inhomogeneities for thicker thin films. The micrometer-thick perovskite thin films exhibit remarkably long charge carrier lifetimes, highlighting their excellent optoelectronic characteristics. They are particularly promising for next-generation inkjet-printed perovskite solar cells, photodetectors, and X-ray detectors.

devices,^[1–3] lasers,^[4,5] photodetectors,^[6] X-ray detectors,^[7–9] and, in particular, photovoltaics (PVs).^[10–14] Recently, power conversion efficiencies (PCEs) exceeding 25% have been demonstrated in perovskite thin film solar cells (PSCs).^[15] The rapid advance of the multicrystalline perovskite thin films builds on excellent optoelectronic properties, namely, strong absorption coefficients,^[16] excellent tolerance to defects, and high charge carrier mobilities.^[17–20] Moreover, given the exceptional ability to tune the band gap of perovskite semiconductor by compositional engineering,^[4,21–23] this class of materials is perfectly suited for realizing tandem solar cells.^[24]

Solution processing of multicrystalline thin films offers an easy and energy-efficient route to manufacture perovskite photovoltaics, given the low crystallization temperature of the perovskite thin films compared to other photovoltaic technologies. Up to date, the research and development of PSCs has been mostly focused on laboratory scale, particularly on spin-coated perovskite thin films.^[10–12,14]

However, with view to a future commercialization of the technology, scalable fabrication of perovskite PV remains a key challenge.^[25] In recent years, research and development of solution-based scalable coating and printing techniques have attracted significant attention, for example, blade coating,^[26,27]

1. Introduction

Within the last decade, hybrid organic–inorganic lead halide perovskite semiconductors have attracted enormous attention in science and technology for lighting-emitting


H. Eggers, F. Schackmar, Dr. T. Abzieher, Prof. U. Lemmer, Prof. B. S. Richards, Dr. G. Hernandez-Sosa, Dr. U. W. Paetzold
Light Technology Institute (LTI)
Karlsruhe Institute of Technology
Engesserstrasse 13, 76131 Karlsruhe, Germany
E-mail: helge.eggers@kit.edu; fabian.schackmar@kit.edu; ulrich.paetzold@kit.edu

H. Eggers, F. Schackmar, Prof. U. Lemmer, Dr. G. Hernandez-Sosa
InnovationLab
Speyerer Strasse 4, 69115 Heidelberg, Germany

H. Eggers, F. Schackmar, Prof. U. Lemmer, Prof. B. S. Richards, Dr. U. W. Paetzold
Institute of Microstructure Technology (IMT)
Karlsruhe Institute of Technology
Hermann-von-Helmholtz-Platz 1, 76344 Eggenstein-Leopoldshafen, Germany

Dr. Q. Sun, Prof. Y. Vaynzof
Kirchhoff Institute for Physics and Centre for Advanced Materials
Heidelberg University
Im Neuenheimer Feld 227, 69120 Heidelberg, Germany

Prof. Y. Vaynzof
Integrated Centre for Applied Physics and Photonic Materials
Centre for Advancing Electronics Dresden (cfaed)
Technical University of Dresden
Nöthnitzer Straße 61, 01187 Dresden, Germany

 The ORCID identification number(s) for the author(s) of this article can be found under <https://doi.org/10.1002/aenm.201903184>.

© 2019 The Authors. Published by WILEY-VCH Verlag GmbH & Co. KGaA, Weinheim. This is an open access article under the terms of the Creative Commons Attribution-NonCommercial License, which permits use, distribution and reproduction in any medium, provided the original work is properly cited and is not used for commercial purposes.

DOI: 10.1002/aenm.201903184

slot-die coating,^[28,29] and inkjet printing.^[30–36] Inkjet printing stands out among these technologies as a noncontact digital printing technique that offers the freedom of printing arbitrary design patterns^[37] at very low material consumption.^[38] Inkjet printing is an adaptable and fast printing technique and is used not only in research on, for example, large-area organic solar cells,^[39] but also already in large-area industrial applications such as next-generation organic light-emitting diode production lines.^[40,41] Over the past years, (partly) inkjet-printed (IJP) PSCs demonstrated continuous increase in PCEs and first studies on the scalability of inkjet-printed perovskite solar cells (IJP PSCs) were reported.^[30–35] Recently Li et al. demonstrated a PCE of over 18% for IJP lead iodide layers that are consequently transformed by a methylammonium iodide evaporation step to methylammonium lead iodide (MAPbI₃).^[35] In addition, Liang et al. used a one-step inkjet printing process for MAPbI₃ to obtain similar PCEs of over 17% on small area (0.04 cm²).^[34] Moreover, IJP PSCs have demonstrated concepts for colorization.^[42]

Despite the progress on IJP PSCs, the PCEs and stable power outputs of these devices lack significantly behind the state-of-the-art spin-coated PSCs.^[25,43] To date, the progress on IJP PSCs has been largely based on adapted recipes and process parameters from spin-coated PSCs, for example, with regard to precursor systems, device architecture, and annealing procedures.^[30,32,33,44–46] In order to close the gap in performance, three key challenges need to be addressed regarding the processing of IJP PSCs: First, achieving optimal printability of perovskite thin films by inkjet printing requires engineering of the solvent composition, whereby all the precursor materials are dissolved in a so-called ink.^[47–49] Second, the underlying charge transport layer not only needs to enable optimal charge carrier extraction, but it also needs to support optimal wetting of the printed ink droplets. This optimization requires ongoing engineering of the ink–surface interaction (e.g., by means of surface treatment) along with optimizations of the layer stack.^[36,46] Third, for high performance PSCs, the nucleation and crystallization of the deposited perovskite wet films needs to be controlled.^[50,51] For spin-coated perovskite thin films, the so-called anti-solvent treatment is an established strategy to control crystallization of multi-cation perovskite thin films.^[14,52] However, given the large amounts of solvents required and the very complex timing of the prompt crystallization initiated by the anti-solvent treatment, it needs to be modified or replaced to realize scalable deposition, for example, by a vacuum-assisted crystallization.^[33,53]

In this work, these three challenges are addressed with the objective to optimize PCE and stability of IJP PSCs. In particular, the ink composition, surface treatment, deposition, and annealing methods of IJP perovskite films are presented for different printing parameters. Material characterization reveals the crystal growth, lead iodide content, surface composition, and charge carrier lifetimes. IJP multicrystalline perovskite absorber layers with large columnar crystals are deposited, exhibiting grains extending over the entire layer thickness. With increasing printing resolution, hence thickness, the perovskite films demonstrate lower relative lead iodide content and longer charge carrier lifetimes. Interestingly, PSCs fabricated using IJP perovskite thin film absorbers (exemplary stack in **Figure 1a**) perform better for layer thicknesses significantly higher than for comparable state-of-the-art spin-coated devices.

Champion devices with a thickness of around 1.5 μm exhibit a single scan PCE of >21% (**Figure 1b**), a stabilized PCE of up to 18.5% (**Figure 1c**), and show no significant drop in PCE after 72 h (**Figure 1e**). Throughout the detailed characterization of the underlying nickel oxide (NiO_x) layer the stabilized PCE has been published earlier this year.^[36] The demonstrated short-circuit current density (J_{SC}) of these IJP PSCs is in the range of the highest J_{SC} reported for spin-coated PSCs of similar architecture and same band gap^[10,12,13] as well as, to the authors' best knowledge, considerably higher than any IJP PSCs.^[25] This improvement originates from exceptionally thick absorber layers, compared to state-of-the-art spin-coated and excellent charge carrier lifetimes. In addition, open-circuit voltage (V_{OC}) and fill factor are remarkably high, inter alia indicating that the IJP perovskite thin film exhibits high diffusion lengths. The PSCs demonstrated in this work show low hysteresis (champion device's hysteresis index factor (HIF) is 0.84; see the Experimental Section), which is remarkable for IJP PSCs.^[31,46] The presented results are the highest stabilized PCE for IJP PSCs and both PCE and stabilized PCE are considerably closer to state-of-the-art values achieved with spin-coating than any preceding reports (**Figure 1d**).^[25,32,54,55]

2. Manufacturing of Inkjet-Printed Solar Cells

2.1. Fabrication of Perovskite Solar Cells

The perovskite solar cells reported in this study are processed in the *p-i-n*-architecture based on the layer sequence glass/indium tin oxide (ITO)/NiO_x/perovskite/C₆₀/bathocuproine (BCP)/gold as depicted in **Figure 1a** (for a detailed description of the fabrication process see the Experimental Section). Prepatterned ITO-coated glass substrates were coated with NiO_x as hole transport layer (HTL) deposited by electron beam evaporation as described in detail by Abzieher et al.^[36] Subsequently, the triple-cation mixed halide perovskite (TCP) absorber layers were deposited. The reference spin-coated samples were prepared using the widely established anti-solvent step and consecutive annealing on a hotplate in an inert nitrogen atmosphere.^[52,56] The IJP samples were processed under controlled ambient conditions (relative humidity of ≈45%). The key steps of the process of the perovskite thin film are depicted in **Figure 2** and described in detail in the following section. The solar cells were completed by evaporating a C₆₀ fullerene electron transport layer on top, followed by a 3 nm thin BCP interfacial layer. Finally, a gold rear electrode is thermally evaporated using a shadow mask, which defines the active area to 10.5 mm².

2.2. Inkjet-Printed Triple-Cation Perovskite Thin Films

Fabrication of high performance IJP perovskite thin films involves three key steps, as shown in **Figure 2**: (1) Ink preparation: the ink needs to be engineered such that ink droplets of well-defined size and shape are generated with a given ink system; (2) Inkjet printing: the droplets have to be printed on the substrate, where the forces between ink (cohesion of the droplet) and substrate (adhesion to the surface) need to be balanced to avoid repelling on the one side and uncontrolled

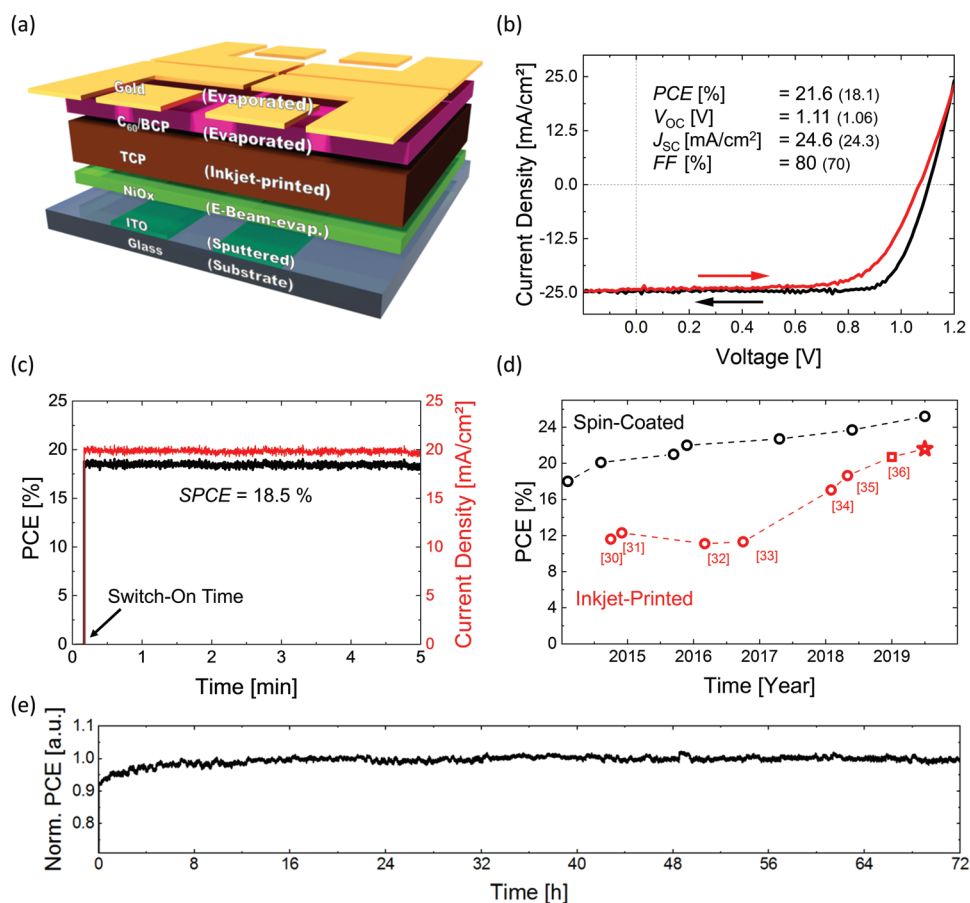


Figure 1. a) Schematic of small-area perovskite solar cell (PSC) stack with deposition methods for each layer. b) Current–voltage (J – V) characteristics of champion solar cell with inkjet-printed (IJP) triple-cation perovskite (TCP) absorber layer. Photovoltaic parameters of champion IJP PSC derived from backward (forward) J – V characteristics. c) Stabilized power conversion efficiency (SPCE) of champion solar cell measured at constant voltage for 5 min as shown before in Abzieher et al.^[36] The switch-on time of the light source is marked, showing the behavior of the PSC in the seconds after illumination. d) Comparison of this work's champion PCE (marked as star) with best PCEs of IJP PSCs reported in literature so far, including the results of the previous publication (marked as square).^[30–36] For the comparison neither solar cell area nor architecture was considered. For reference, the record PCEs for spin-coated PSCs are also given for the same time frame.^[15] e) SPCE measured over 72 h by maximum power point tracking. Values were normalized to the average of 100 min after 1000 min taking a visible light soaking effect into account. Not the same PSC as shown in (c).

spreading over the whole substrate on the other side; and (3) Drying and annealing: the solvents in the as-printed wet films need to evaporate and the remaining precursor materials need to crystallize in a pinhole-free perovskite thin film.

2.2.1. Ink Preparation

As the printing setup used in this work only allows for a single channel print process, a single ink approach is presented. Although without multichannel the perovskite composition cannot be changed during printing, the single channel approach makes the process accessible to a large variety of inkjet printing setups with similar constraints. Hence, we prepare a single ink for deposition of TCP thin films, containing cesium (Cs), methylammonium (CH₃NH₃, MA), and formamidinium (CH(NH₂)₂, FA), similar to Mathies et al.^[46] The targeted stoichiometric ratio of the TCP perovskite thin films is Cs_{0.1}MA_{0.15}FA_{0.75}Pb(I_{0.85}Br_{0.15})₃. For this, the precursor materials (see the Experimental Section) are dissolved in a mixed

solvent system. In our studies a mixture of the high-boiling-point solvent γ -butyrolactone (GBL) and the polar-aprotic solvents *N,N*-dimethylformamide (DMF) as well as dimethyl sulfoxide (DMSO) resulted in improved homogenous drying. The excellent droplet formation of this ink system is shown in Figure S1 of the Supporting Information.

2.2.2. Inkjet Printing

The droplets ejected from the print-head of the inkjet printing system impinge next on the substrate. In inkjet printing wetting behavior of the droplets on the substrate surface is classified as de-wetting, over-wetting, and optimal wetting. While the first describes the contraction of the as-printed droplets on the surface without formation of a continuous wet film, the second describes the inhomogeneous spread of droplets across the substrate with in the worst case no pinning behavior. In order to achieve optimal (partial) wetting behavior, a minimum contact angle θ of about 5°–10° between the droplet and the

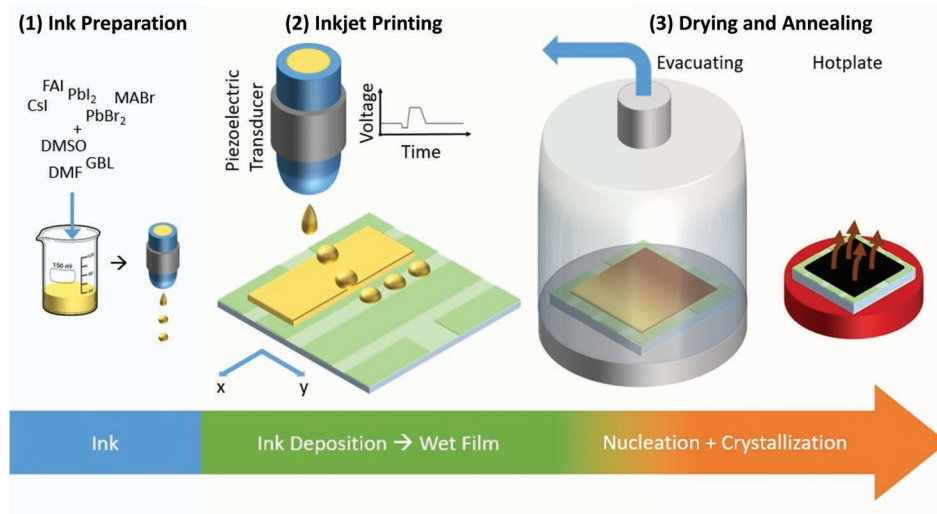


Figure 2. Schematic illustration of the key steps involved in inkjet printing of triple-cation multicrystalline perovskite (TCP) thin films: (1) Ink preparation: Solvent system-engineering of the perovskite precursor solution to get a printable ink. (2) Inkjet printing: Drop-on-demand inkjet printing process, whereby a waveform applied to a piezoelectric transducer controls the ejection of individual ink droplets. The overlapping droplets printed on the substrate coalesce and form a wet film. The printed resolution determines the amount of ink deposited and thereby the layer thickness. (3) Drying and annealing: The printed TCP wet film is transferred to a vacuum chamber to increase the evaporation rate of the solvents and induce nucleation of the perovskite thin film. The crystallization of the perovskite thin film is initiated and the chamber is vented. The perovskite crystallization is completed in a final annealing step on a hot plate.

substrate surface is needed to avoid over-wetting. On the other hand, $\theta < 90^\circ$ is the theoretical upper limit, since the droplets start to repel from the surface, which leads to de-wetting. To tune the contact angle, the surface tension (SFT) of the ink and the surface free energy (SFE) of the substrate need to be adjusted. To estimate the wettability of the TCP ink on the NiO_x-coated substrate, the polar and dispersive part of the SFE are calculated according to the Owens, Wendt, Rabel, and Kaelble (OWRK) method, using contact angle measurements from four different solvents with known polar and dispersive SFT parts (see the Experimental Section for details).^[57–59]

The so-called wetting envelope, which displays a line of constant contact angle (i.e., $\theta_{\text{envelope}} = 0^\circ$) for a given substrate, is depicted in **Figure 3a**. Combined with the dispersive and polar part of the SFT, the wetting envelope allows to assess the wetting of a solvent system on a specific substrate: For $\theta_{\text{envelope}} = 0^\circ$, the SFT inside the envelope should lead to complete wetting. The more the SFT shifts from the wetting envelope toward higher values, the larger the contact angle, leading ultimately to an entire de-wetting. In agreement with the depicted wetting envelopes in **Figure 3**, the NiO_x HTL used in this work leads to contact angles $\theta > 25^\circ$ that imply small droplet diameters

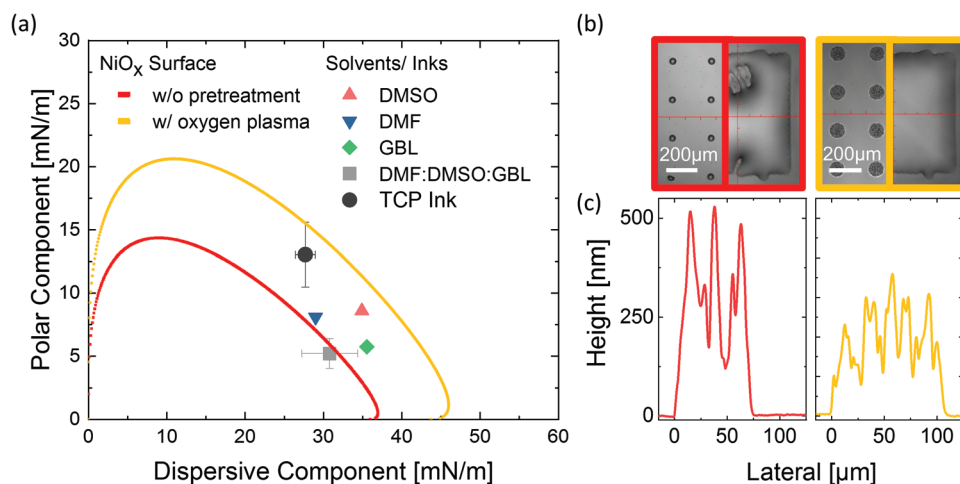


Figure 3. a) Wetting envelopes (line of constant contact angle $\theta = 0^\circ$ depending on the polar and dispersive parts of the surface free energy) of NiO_x layers with and without oxygen plasma treatment and the polar and dispersive part of the surface tension of the solvents and ink used in the process. Calculated according to the OWRK theory based on measured contact angles. b) Corresponding top-view microscopic images of the IJP droplets and IJP areas depending on the surface treatment of the NiO_x layer. c) Corresponding profile shapes of dried droplets depending on the surface treatment of the NiO_x layer.

(see Figure 3b). Although it is possible to print on surfaces with contact angles of $\theta \approx 25^\circ$, often an increased density of (pin-)holes due to local de-wetting (see Figure S2 in the Supporting Information) is observed for this range of angles for IJP perovskite thin films. To minimize the de-wetting, a short low-power oxygen plasma is applied prior to the printing process to increase the overall SFE in a way that the SFT of the ink lies inside the envelope. Although this does not exactly match the theory (it should be $\theta_{\text{theory}} < \theta_{\text{envelope}}$, but it is $\theta \approx 10^\circ > \theta_{\text{envelope}}$), the wetting improves, which results in larger drop diameters and increases the feature size ($\approx 100 \mu\text{m}$ instead of $\approx 70 \mu\text{m}$; see Figure 3b), and thus reduces the risk of formation of holes in the wet film significantly (see Figure S2 in the Supporting Information). Although the demonstrated droplet diameters of $100 \mu\text{m}$ are rather large, we are still able to print almost arbitrary patterns even on relatively small scales with sub-millimeter structures with this process (Figure S3 in the Supporting Information).

2.2.3. Drying and Annealing

Subsequent to the printing of the wet film, the samples are moved manually to a nearby vacuum chamber. Since the wet film is of significant thickness ($\approx 20 \mu\text{m}$ for 1100 dots per inch (dpi), calculated), the samples have to be moved with care to avoid movement of the wet-film profile. The vacuum chamber is evacuated for a few minutes. While the pressure is going down to 5×10^{-2} mbar, the boiling point of the solvents decreases and the evaporation rate of the solvents increases. According

to the ascending boiling point, DMF starts to evaporate first, followed by DMSO and GBL. While the solvents are getting extracted, the shrinking wet film starts to crystallize, indicated by a change in color from yellow to dark brown. After that, the chamber is slowly vented with ambient air and the samples are subsequently annealed on a hotplate under ambient air.

3. Results

3.1. Inkjet-Printed Perovskite Thin Films with Large Columnar Grains

The PSCs with IJP multicrystalline perovskite absorber layers introduced in Figure 1 exhibit an exceptional thickness around $1.5 \mu\text{m}$ along with high PCEs and stable power outputs. In order to investigate the morphology and the optoelectronic characteristics of the micrometer-thick IJP perovskite layers, their thickness along with the printing resolution—given in dpi—is varied.

Scanning electron microscopy (SEM) images of the cross-section of the perovskite layers, shown in Figure 4a, provide an estimate of the respective thicknesses, which are in good agreement with the profilometer measurements that are used to determine the actual thickness. The layer thickness increases approximately quadratic with the printing resolution, as expected by theory and described in previous reports.^[46] The perovskite thin film thickness ranges from $\approx 400 \text{ nm}$ (600 dpi) up to almost $4 \mu\text{m}$ (2000 dpi). It should be noted that such

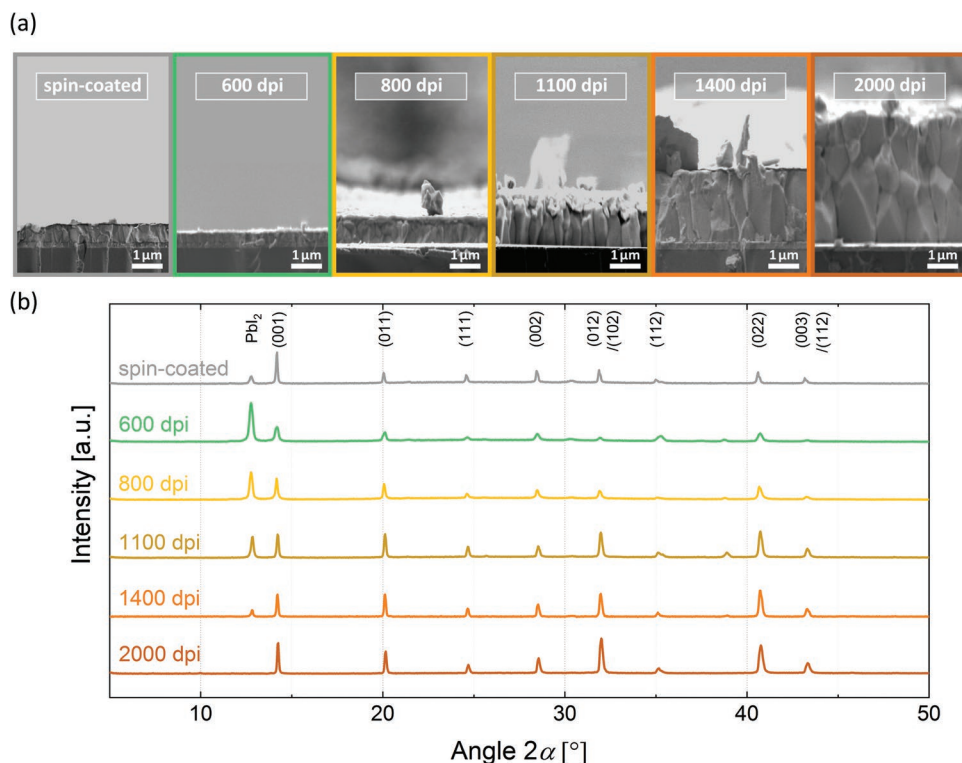


Figure 4. a) Scanning electron microscopy (SEM) images of cross-sections of perovskite solar cells with IJP perovskite absorber layers printed with different resolutions. A spin-coated reference is shown as well. b) X-ray diffraction (XRD) diffractogram and of IJP perovskite layers (and a spin-coated reference) processed on the substrate glass/ITO/NiO_x.

thick perovskite thin films cannot be deposited by spin-coating, where spin speed and solubility limit the thickness. Much thinner layers are also commonly used for state-of-the-art PSCs processed with alternative scalable fabrication techniques, e.g., 500–600 nm for blade coating,^[26,60] 350–430 nm for slot-die coating,^[29,61] or 350 nm for thermal co-evaporation.^[36,62] In previous reports on PSCs with perovskite absorber thin films deposited by inkjet printing, horizontal grain boundaries are apparent, introducing defects that induce nonradiative recombination and impede the charge transport through the absorber.^[46] In contrast, the IJP perovskite thin films of this work exhibit large columnar grains extending over the entire perovskite thin film even for the thickest layers (over 4 μm) examined in this work (see SEM images of the layer cross-sections in Figure 4a). This allows for perovskite absorber layers with only few to no horizontal grain boundaries, improving its transport properties. SEM images of the perovskite surface indicate an increasing grain size for higher resolutions in horizontal directions (compare Figure S5 in the Supporting Information), suggesting a similar trend as observed for the formation of the vertical grains (Figure 4a).

To further investigate the influence of inkjet printing with different printing resolution, as well as the differences in annealing on the formation of the perovskite thin films, stacks of glass/ITO/ NiO_x and perovskite were investigated by X-ray diffraction (XRD) (Figure 4b). The XRD diffractograms exhibit diffraction peaks for the perovskite in both the printed layers and the spin-coated reference, including the prominent diffraction peak of the (001)-plane of the cubic perovskite phase at 14.2° and the combined peak of the (012) and (102)-plane at $\approx 32^\circ$.^[63] However, the relative intensity of the peaks assigned to different crystal planes of the perovskite crystal structure systematically changes with the thickness of the perovskite thin film. For example, compared to the (001)-peak, the (012)-/(102)-peak grows disproportionately from a 4:1 ratio for 600 dpi to less than a 1:1 ratio for 2000 dpi (2.5:1 for the spin-coated reference). This indicates that crystallization along either the (012) or (102)-plane is increasingly dominant with thicker layers supporting the observation of a change in preferred crystal orientation made by SEM.

Not only the preferred crystal orientation, but also the overall composition of the perovskite changes: spin-coated layers show a significantly lower lead-iodide-to-perovskite ratio than printed layers of comparable thickness (600–800 dpi), which can be determined by comparison of the diffraction peak attributed to lead iodide (12.8°) and the diffraction peak attributed to the perovskite (100)-plane (see Figure 4b). This indicates an enhanced lead iodide volume fraction in the IJP perovskite layers, which is attributed to the differences in the fabrication process, for example a significantly slower vacuum annealing step compared to anti-solvent treatment for spin-coated perovskite thin films as well as a modified solvent system. Furthermore, it should be noted that the lead-iodide-to-perovskite ratio decreases with increasing printing resolution. On the one hand, this could indicate an overall different crystal composition, for example, due to slower drying of the thicker wet films printed with high resolutions. On the other hand, this could also point to local differences in crystallization: since higher printing resolution entail thicker thin films this is an indication

of lead-iodide-rich layers forming at a perovskite interface (with either the underlying HTL or air) that decreases in volume fraction with increasing thin film thickness.

It should be further noted that the roughness of IJP perovskite thin films increases with printing resolution and is significantly higher compared to spin-coated thin films, due to the absence of a centrifugal force and a slower drying process (see above) giving rise to fluid mechanically driven artifacts, such as coffee rings (compare Figure S4 in the Supporting Information). In order to investigate the composition at the surface of these IJP perovskite thin films, spatially resolved X-ray photoemission spectroscopy (XPS) mapping was conducted. The investigated layer stack represents an uncompleted PSC (glass/ITO/ NiO_x /TCP). The XPS maps display the atomic ratios of cesium, nitrogen (originating from the MA and FA cations), iodine, and bromine in comparison to lead over an area of $8 \times 8 \text{ mm}^2$ (Figure 5a). The more uniformly colored maps observed for printing resolutions of 600–1100 dpi indicate fewer local differences in the surface composition of the films and therefore, an overall more homogeneous layer. Figure 5b summarizes the distribution of the element ratios (Cs/Pb, N/Pb, Br/Pb, and I/Pb) measured at the perovskite surface. The decrease in homogeneity of the perovskite composition at the surface with increasing printing resolution is apparent as a broadening of all elemental ratio distributions. Not only are the perovskite thin-film surfaces printed with 600–1100 dpi the most homogeneous, but for these layers the average composition of the surface also deviates less from the desired perovskite composition of $\text{Cs}_{0.1}\text{MA}_{0.15}\text{FA}_{0.75}\text{Pb}(\text{I}_{0.85}\text{Br}_{0.15})_3$. In this context it should be noted that for all element ratios a small lead deficiency is observed, which is in agreement to other XPS studies.^[64–68] Very thick ($>1.5 \mu\text{m}$) perovskite thin films processed with higher resolution (1400 and 2000 dpi) are significantly more inhomogeneous and contain significant excess of halides, cesium, and organic cations at the surface than the films deposited at lower resolution.

Having investigated the stoichiometric composition and crystallinity, next the good optoelectronic quality of the thick IJP perovskite thin films is highlighted by photoluminescence (PL) measurements. A two-term exponential fit (see the Experimental Section for details) was used to determine a mixed time constant τ_1 and a charge carrier lifetime constant τ_2 as decay constants of time-resolved PL on perovskite thin films on glass/ITO/ NiO_x (Figure 6).^[69–72] While the charge extraction time constant is similar for all samples, layers printed with higher resolutions (especially 1100 dpi and more) display significantly longer charge carrier lifetime constants, emphasizing the excellent optoelectronic quality. This is attributed to the formation of large columnar grains extending over the entire thin film thickness, minimizing the influence of crystal domain grain boundaries that are prone to recombination centers and non-radiative recombination. The comparison of spin-coated to low resolution-printed films with comparable thickness (600 dpi) shows similar lifetime constants, which suggests that the changes in relative lead iodide content seen in XRD are in this case not detrimental for the changed charge carrier transport.^[71] A comparison with PL measurements on perovskite layers inkjet printed on glass (Figure S6, Supporting Information) suggests that while quenching at the NiO_x interface is an

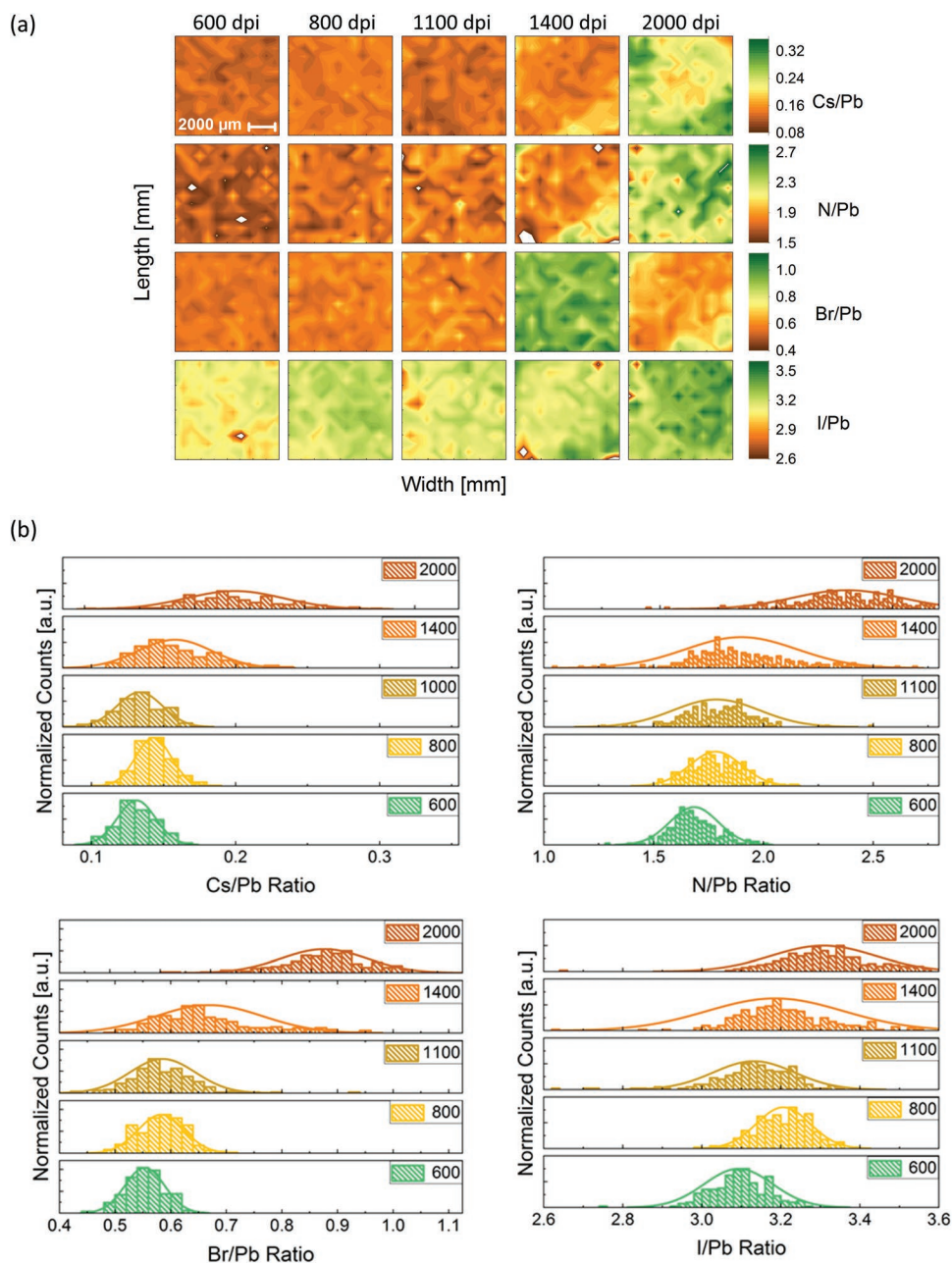


Figure 5. a) Local distribution of element ratios at the perovskite surface determined by spatially resolved X-ray photoemission spectroscopy (XPS) mapping of IJP perovskite on glass/ITO/ NiO_x stacks. Mapping area is $8 \times 8 \text{ mm}^2$ for each sample. Different printing resolutions for the IJP perovskite are displayed in the columns. Four elemental ratios (Cs/Pb, N/Pb, Br/Pb, and I/Pb) are shown in the rows. b) Statistical analysis of the XPS maps.

observable effect, it is not the dominant mechanism behind the change of lifetime constant τ_2 . It should be highlighted that the charge carrier lifetime constant in the thicker perovskite thin films (1100–2000 dpi) is in the range of 0.5–1 μs , which is a truly remarkable value in view of lifetimes reported previously for multicrystalline perovskite thin films (up to values of 480 ns for triple-cation perovskites, including determination with a two-term exponential fit^[72,73]) and proving the exceptional optoelectronic quality of printed perovskite films presented in this work.

3.2. Perovskite Solar Cells with Inkjet-Printed Layers

Considering the long lifetimes of the thick IJP perovskite layers with large columnar grains, the performance of IJP PSCs is investigated next. Although theoretical expectations of diffusion lengths for electrons and holes in perovskite range up to 1 μm and above,^[20] for most state-of-the-art spin-coated PSCs an absorber thickness of around 400–600 nm has proven to result in most efficient devices. Likewise, many works published so far on PSCs via inkjet printing report

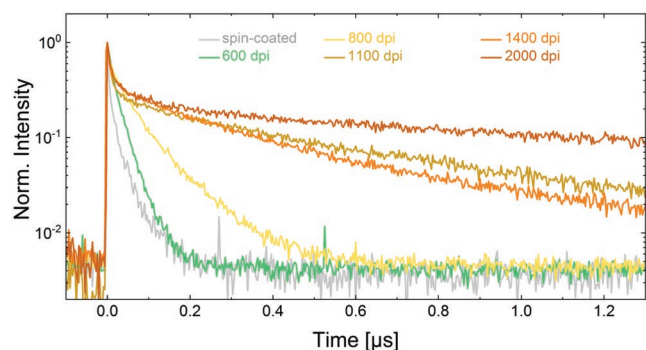


Figure 6. Time-resolved photoluminescence (PL) of IJP perovskite layers (and a spin-coated reference) processed on the layer stack glass/ITO/NiO_x.

PCE-maxima for similar thickness.^[34,46] Therefore, the performance of IJP PSC with different layer thicknesses, achieved by variation of printing resolution, is compared here. With increasing printing resolution, thus thickness, an optimal point of performance becomes apparent at 1100 dpi (roughly 1.5 μm layer thickness), which can be related to the material and layer properties investigated by SEM, PL, XRD, and XPS

measurements (**Figure 7**): While the fill factor is the highest for devices printed with low resolution, the short-circuit current density J_{sc} increases with resolution up to a maximum of 24 mA cm⁻² for 1100 dpi, respectively 1.5 μm, which is similar to a calculated thickness with maximum J_{sc} for low recombination regime MAPbI₃ of 1.3 μm.^[74,75] As detailed above, the increase in J_{sc} in the devices is attributed to the excellent charge carrier lifetimes measured and the low number of horizontal grain boundaries of the columnar crystal grains extending over the thin film (compare Figure 4a) and increases significantly up to this resolution. Additionally, with increasing resolution the volume ratio of lead iodide compared to perovskite in the thin film is decreasing, which is assumed to be beneficial for the device. For layers printed with higher resolutions (1400–2000 dpi), both current density and fill factor decrease significantly (Table S7, Supporting Information). According to the material characterization two possible reasons for this can be identified: First, such high printing resolutions entail perovskite thin film thicknesses of up to 4 μm. In spite of the exceptional long charge carrier lifetimes, efficient charge transport over the entire thickness might not be possible anymore. Second, the perovskite thin-film surface gets less homogeneous and differentiates more

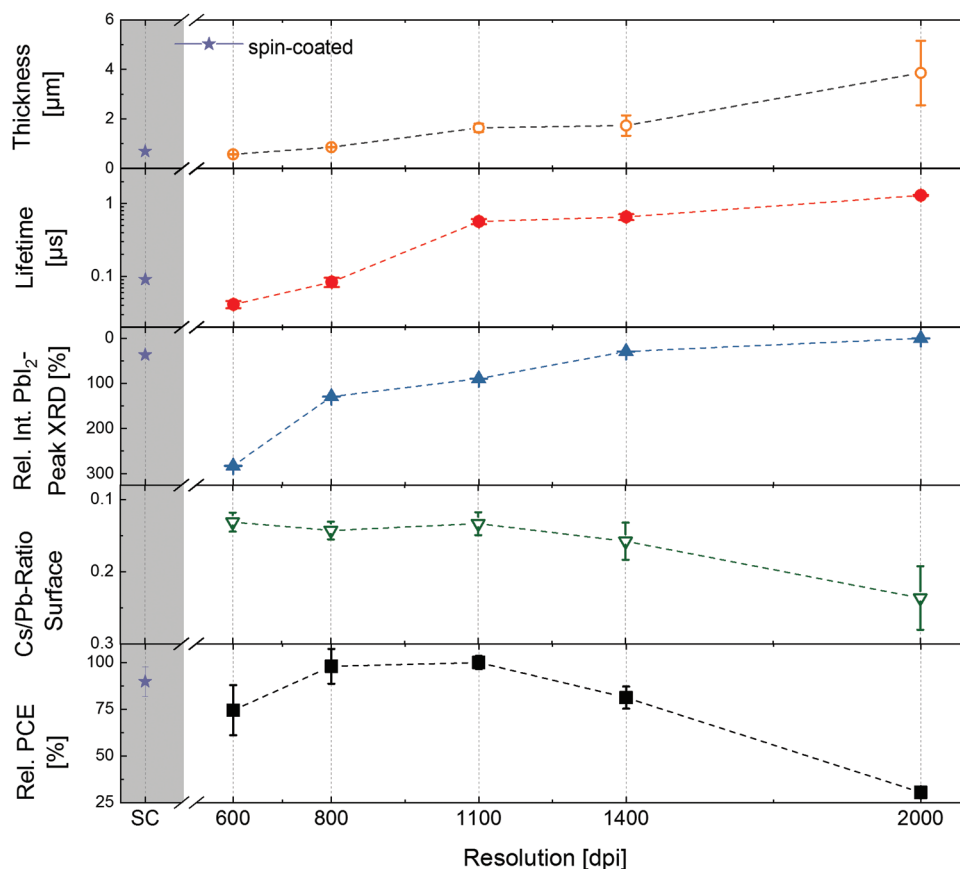


Figure 7. Overview over layer thickness, charge carrier lifetime constant, relative intensity of the XRD lead iodide peaks (compared to the (100) perovskite plane), stoichiometric ratio of cesium to lead at the perovskite surface, and relative PCE of perovskite layers deposited by IJP with different printing resolutions or entire solar cells with these layers for the PCE, respectively. Values for a spin-coated layer/all-spin-coated device were added as reference. Error bars indicate the standard deviation for thickness, lifetime, elemental surface ratio, and relative PCE and in case of the relative intensity of the XRD peaks the square root of sum of squares of standard deviations of both single peaks.

from the desired stoichiometric composition influencing the charge carrier extraction.

There is an optimal printing resolution for IJP PSC that results from a trade-off between: i) increasing lifetime as well as decreasing lead-iodide ratio; and ii) increasing thickness and decreasing surface quality. The maximum PCE is identified for devices with IJP perovskite layers with a printing resolution of about 1100 dpi. This corresponds to a thickness of roughly 1.5 μm . Simple drop-coating experiments with similar ink-volume, which should mimic the deposition by inkjet printing, demonstrate a similar trend, affirming a correlation between PCE and thin film thickness. However, a wide statistical spread in performance of drop-coated devices compared to IJP ones is observable, presumably since especially area and therefore wet-film thickness is harder to control. Best IJP devices allow for maximum PCEs of over 21% in backward J - V characteristics and average PCEs of almost 20% (best: 19.9%). To the best of the authors' knowledge, this is the highest PCE for IJP perovskite layers so far. The hysteresis effect is, on average, lowest for devices fabricated with 1100 dpi printing resolution (compare HIF in Table S7 in the Supporting Information). However, it is not negligible. Hence, an average PCE or as chosen here the stabilized PCE under maximum power point (MPP) tracking is more meaningful to evaluate the solar cell performance. The maximum short-time stabilized PCE is 18.5%. High-performance PSCs were reproducibly fabricated over seven batches with an average single-scan PCE of $16.3\% \pm 2.5\%$ for 178 solar cells (see Figure S9 in the Supporting Information). Although the average is considerably lower than the best PCE, this is a result with significant impact, since addressing the problems with reproducibility and stability of devices is essential for commercialization not only for IJP PSCs but also for PSCs in general. Here, solar cells with thick absorber layers might also be of advantage, since the probability of short-circuits through formation of pinholes significantly decreases with thickness leading to fewer shunted devices per batch and assumable to reduced material degradation facilitated by pinholes. To provide proof-of-concept for scalability, an immature prototype of a PSC with active area of $\approx 1 \text{ cm}^2$ was fabricated (see Figure S10 in the Supporting Information). The mean PCE of 10.4% is mainly limited by a low fill factor, which is assumed to origin in a non-optimized layout. V_{OC} and J_{SC} are comparable to the standard devices.

3.3. Conclusion

Here, we demonstrate IJP PSCs with a PCE of over 21% and also exhibiting $>18\%$ stabilized PCE—both of these values are the highest reported for partly IJP PSCs so far—as well as good reproducibility. Champion devices incorporate very thick absorber layers of about 1–1.5 μm (printing resolution 1100 dpi). The IJP perovskite thin films exhibit columnar perovskite crystal structures that extend over the entire thickness without horizontal grain boundaries, as evidenced via scanning electron microscopy. These columnar perovskite crystal structures are assumed to have few defects and facilitate efficient charge carrier transport. In addition, the printed perovskite thin films show long charge carrier lifetimes of $>0.5 \mu\text{s}$, proven by

time-resolved photoluminescence measurements. Although an effective decrease of relative PbI_2 amount in the perovskite for thicker layers by X-ray diffraction is observable, X-ray photo-emission spectroscopy studies indicate that only layers up to $\approx 1.5 \mu\text{m}$ thickness exhibit the desired surface composition with a high degree of homogeneity. This work demonstrates that the PSCs with IJP triple-cation absorber can be close to PCE of state-of-the-art devices by other deposition methods, enabling this material-efficient process, which is well suited for upscaling while additionally offering the possibility to process in almost arbitrary patterns.

In view of the future development of the technology, this study provides a remarkable demonstration that very thick perovskite absorber layers that are possibly easier to scale up without defects can be deposited at high quality by inkjet printing.

4. Experimental Section

Sample Fabrication: For preparation of the samples, the following route was used: Prepatterned ITO on glass substrates (Luminescence Technology) were cleaned consecutively in acetone and isopropanol in an ultrasonic bath for 10 min each, followed by an oxygen plasma-cleaning step for 2–3 min. Afterward 20 nm NiO_x HTL was deposited as described in detail by Abzieher et al.^[36] Basically, green raw material NiO_x lumps (Alfa Aesar, 99.995%) were filled into an alumina crucible in an electron evaporation system (Angstrom Engineering) and were evaporated at base pressures around 10^{-6} mbar, while using a small (about 10 sccm) oxygen flow to maintain the original composition ratio.

Subsequently, the TCP absorber layers were deposited. The ink for inkjet printing was prepared as follows: $\text{CH}(\text{NH}_2)_2\text{I}$ (FAI, 0.6 M, GreatCell Solar), PbI_2 (0.66 M, TCI Chemicals), $\text{CH}_3\text{NH}_3\text{Br}$ (MABr, 0.12 M, GreatCell Solar), and PbBr_2 (0.12 M, TCI Chemicals) were dissolved in a mixture of DMF (Sigma-Aldrich), DMSO (Merck), and GBL (Sigma-Aldrich) in a ratio of 28:26:46 (volume percentage). Additionally, CsI (1.5 M, Alfa Aesar) was dissolved in DMSO and then added to the first solution to get a 0.75 M TCP solution with the composition $\text{Cs}_{0.10}\text{FA}_{0.75}\text{MA}_{0.15}\text{Pb}(\text{Br}_{0.15}\text{I}_{0.85})_3$. Before printing, the ink was filtered with a 0.45 μm pore size polytetrafluoroethylene (PTFE) filter. The triple-cation solution for spin coating was prepared with the same precursor salts (FAI 1 M, PbI_2 1.1 M, MABr 0.2 M, and PbBr_2 0.2 M) in a mixture of DMF and DMSO in a ratio of 4:1 (volume percentage). The same CsI 1.5 M solution was then added to achieve a $\text{Cs}_{0.10}\text{FA}_{0.75}\text{MA}_{0.15}\text{Pb}(\text{Br}_{0.15}\text{I}_{0.85})_3$ composition.

For inkjet printing of the TCP layers, a Meyer Burger PiXDRO LP50 with a print head module for 10 pl Fujifilm cartridges (Dimatix DMC-16610) was used. Prior to the printing, the NiO_x surface was treated with a short oxygen plasma at low power. For every printed resolution, a jetting frequency of 2 kHz was used together with a single pulse waveform with a peak voltage of 33 V and a pulse width of 5 μs . The total area of inkjet-printed TCP was $12 \times 12 \text{ mm}^2$ per sample. Within the time frame of 30 s the as-printed samples were moved by hand to a nearby vacuum chamber (Pfeiffer Vacuum Technology AG) which was evacuated down to about 5×10^{-2} mbar. Then, the chamber was slowly vented and the samples were annealed on a hotplate at 100 $^\circ\text{C}$. The complete printing procedure was done in ambient atmosphere ($\approx 23 \text{ }^\circ\text{C}$, $\approx 45\%$ relative humidity). For spin coating of the TCP layers, the NiO_x samples were also treated with a short oxygen plasma and then moved into a nitrogen filled glove box. The layer was spin-coated using a two-step program (1000 rpm for 10 s, 5000 rpm for 20 s) with a chlorobenzene (Sigma-Aldrich) anti-solvent step (100 μL) and then annealed for 1 h on a hotplate at 100 $^\circ\text{C}$.

For completing the p - i - n -solar cell stack, a 25 nm thick C_{60} fullerene electron layer, followed by a 3 nm thick BCP interfacial layer, was thermally evaporated on top of the perovskite layer. Finally, a 60 nm

thick gold back contact was thermally evaporated using a shadow mask, which defined the active area to 10.5 mm² per solar cell with four cells per sample.

Characterization—SEM: SEM images were taken with a Zeiss Auriga system. Measurements were taken in high vacuum. For cross-sections, samples were cut on the rear side and broken. Pictures were not corrected for small tilts or errors due to breaking. Since the integration time of pictures may also have a small effect (due to shifts caused by electrical charging and discharging) on the displayed scale, these pictures were not reliable for thickness determination.

Solar Cell Characteristics: For the measurement of the solar cell characteristics, a xenon-lamp-based solar simulator (Newport Oriol Sol3A) inside a nitrogen filled glove box with an AM1.5G spectrum (100 mW cm⁻²) was calibrated with a KG5 short pass-filtered silicon reference solar cell. The cells were then measured in both backward and forward direction with a constant scan rate of circa 0.6 V s⁻¹ (Keithley 2400 source measurement unit) while holding the temperature of the solar cell at 25 °C with a microcontroller-adjusted Peltier element. The MPP was tracked by using a perturb-and-observe method. HIF was calculated as fraction of PCE measured in backward and forward direction: $HIF = PCE_{FW}/PCE_{BW}$.

Time-resolved PL: For the time-resolved photoluminescence measurements, a self-made PL setup with a pulsed laser (532 nm, 5 kHz repetition rate, 800 ps pulse width, 0.5–2 nJ (respectively 100 nJ) for the Supporting Information) pulse energy), an ACTON spectrometer, and a CCD camera (PIMAX512) with a gated mode was used, while keeping the samples in ambient atmosphere. For the evaluation of the PL measurements three main processes were assumed: (1) Recombination with trap states (Shockley–Read–Hall) on the timescale of microseconds, (2) band-to-band recombination on short time scales (<0.1 μs), and (3) quenching of PL by extraction of holes. A two-term exponential fit was used to determine a lifetime constant τ_2 , which was dominated by the process (1) and a second time constant, here called mixed time constant τ_1 , which was dominated by process (2) and (3): $I = a_1 \exp(-t/\tau_1) + a_2 \exp(-t/\tau_2)$. It has to be mentioned that since process (2) and (3) cannot really be described throughout an exponential decay function, this is only a rough estimation for the short time scales.

X-ray Diffraction (XRD): The X-ray diffraction patterns were measured using a Bruker D2 PHASER (Cu K- α radiation).

XPS Mapping: Samples for XPS mapping experiments were prepared as described above and transferred to the ultrahigh vacuum chamber of the XPS system (Thermo Scientific ESCALAB 250Xi). XPS measurements were performed using a XR6 monochromated Al K- α source ($h\nu = 1486.6$ eV) and a pass energy of 20 eV.

Surface Profiles and Thickness: The thickness of the perovskite films was measured using a Bruker Dektak XT profilometer.

Contact Angle, SFE, and SFT: For calculating the wetting envelope and therefore the polar and dispersive part of the SFE of the substrates, the contact angle of four solvents (deionized water, diiodo methane, dimethyl sulfoxide, and ethylene glycol) was measured using a sessile drop method (Krüss DSA 100 drop shape analyzer system). Droplets ($\approx 1\text{--}5$ μL) were set onto the surface and then measured after a short settling time. The polar and dispersive SFE were calculated using Owens–Wendt–Rabel–Kaelble theory using a least absolute residual method. The dispersive and polar part of the SFT of the inks were calculated with the total SFT, measured with the pendant drop method, and the measured contact angles on a PTFE substrate.

Supporting Information

Supporting Information is available from the Wiley Online Library or from the author.

Acknowledgements

The financial support by the Federal Ministry for Research and Education (BMBF) through the project PRINTPERO (03SF0557A), the

Bundesministerium für Wirtschaft und Technologie through the project CAPITANO (3EE1038B), the Initiating and Networking Funding of the Helmholtz Association (HYIG of U.W.P. (VH-NG-1148)); Recruitment Initiative of B.S.R.; the Helmholtz Energy Materials Foundry (HEMF); PEROSEED (ZT-0024); the project HYPer as part of HeiKa research collaboration; and the Science and Technology of Nanostructures Research Program as well as the Karlsruhe School of Optics & Photonics (KSOP) is gratefully acknowledged. The authors would like to thank the members of the Perovskite Taskforce at LTI and the Printed Electronics research group at iL for fruitful discussions and support in their scientific work, especially Dr. Bahram Abdollahi and Pariya Nazari for their help in supporting measurements. In addition the authors would like to express their gratitude toward Dr. Guillaume Gomard for supporting measurements and Marius Jakoby for very helpful discussion on photoluminescence measurements.

Conflict of Interest

The authors declare no conflict of interest.

Author Contributions

H.E. and F.S. contributed equally to this work. The manuscript was written through contributions of all authors.

Keywords

high diffusion lengths, inkjet printing, large columnar crystal grains, perovskite solar cells

Received: September 27, 2019

Revised: November 19, 2019

Published online: December 19, 2019

- [1] Z.-K. Tan, R. S. Moghaddam, M. L. Lai, P. Docampo, R. Higler, F. Deschler, M. Price, A. Sadhanala, L. M. Pazos, D. Credgington, F. Hanusch, T. Bein, H. J. Snaith, R. H. Friend, *Nat. Nanotechnol.* **2014**, *9*, 687.
- [2] E. R. Dohner, A. Jaffe, L. R. Bradshaw, H. I. Karunadasa, *J. Am. Chem. Soc.* **2014**, *136*, 13154.
- [3] W. Xu, Q. Hu, S. Bai, C. Bao, Y. Miao, Z. Yuan, T. Borzda, A. J. Barker, E. Tyukalova, Z. Hu, M. Kawecki, H. Wang, Z. Yan, X. Liu, X. Shi, K. Uvdal, M. Fahlman, W. Zhang, M. Duchamp, J.-M. Liu, A. Petrozza, J. Wang, L.-M. Liu, W. Huang, F. Gao, *Nat. Photonics* **2019**, *13*, 418.
- [4] B. R. Sutherland, E. H. Sargent, *Nat. Photonics* **2016**, *10*, 295.
- [5] P. Brenner, O. Bar-On, M. Jakoby, I. Allegro, B. S. Richards, U. W. Paetzold, I. A. Howard, J. Scheuer, U. Lemmer, *Nat. Commun.* **2019**, *10*, 988.
- [6] H. Wei, Y. Fang, P. Mulligan, W. Chuirazzi, H.-H. Fang, C. Wang, B. R. Ecker, Y. Gao, M. A. Loi, L. Cao, J. Huang, *Nat. Photonics* **2016**, *10*, 333.
- [7] H. Mescher, E. Hamann, U. Lemmer, *Sci. Rep.* **2019**, *9*, 5231.
- [8] Y. C. Kim, K. H. Kim, D.-Y. Son, D.-N. Jeong, J.-Y. Seo, Y. S. Choi, I. T. Han, S. Y. Lee, N.-G. Park, *Nature* **2017**, *550*, 87.
- [9] S. Yakunin, M. Sytnyk, D. Kriegner, S. Shrestha, M. Richter, G. J. Matt, H. Azimi, C. J. Brabec, J. Stangl, M. V. Kovalenko, W. Heiss, *Nat. Photonics* **2015**, *9*, 444.
- [10] E. H. Jung, N. J. Jeon, E. Y. Park, C. S. Moon, T. J. Shin, T.-Y. Yang, J. H. Noh, J. Seo, *Nature* **2019**, *567*, 511.

- [11] W. Tress, K. Domanski, B. Carlsen, A. Agarwalla, E. A. Alharbi, M. Graetzel, A. Hagfeldt, *Nat. Energy* **2019**, *4*, 568.
- [12] D. Luo, W. Yang, Z. Wang, A. Sadhanala, Q. Hu, R. Su, R. Shivanna, G. F. Trindade, J. F. Watts, Z. Xu, T. Liu, K. Chen, F. Ye, P. Wu, L. Zhao, J. Wu, Y. Tu, Y. Zhang, X. Yang, W. Zhang, R. H. Friend, Q. Gong, H. J. Snaith, R. Zhu, *Science* **2018**, *360*, 1442.
- [13] J. A. Christians, P. Schulz, J. S. Tinkham, T. H. Schloemer, S. P. Harvey, B. J. Tremolet de Villers, A. Sellinger, J. J. Berry, J. M. Luther, *Nat. Energy* **2018**, *3*, 68.
- [14] M. Saliba, J. P. Correa-Baena, C. M. Wolff, M. Stollerfoht, N. Phung, S. Albrecht, D. Neher, A. Abate, *Chem. Mater.* **2018**, *30*, 4193.
- [15] NREL, Best Research-Cell Efficiency Chart, <https://www.nrel.gov/pv/cell-efficiency.html> (accessed: September 2019).
- [16] S. De Wolf, J. Holovsky, S.-J. Moon, P. Löper, B. Niesen, M. Ledinsky, F.-J. Haug, J.-H. Yum, C. Ballif, *J. Phys. Chem. Lett.* **2014**, *5*, 1035.
- [17] V. D'Innocenzo, G. Grancini, M. J. P. Alcocer, A. R. S. Kandada, S. D. Stranks, M. M. Lee, G. Lanzani, H. J. Snaith, A. Petrozza, *Nat. Commun.* **2014**, *5*, 3586.
- [18] C. Motta, F. El-Mellouhi, S. Sanvito, *Sci. Rep.* **2015**, *5*, 12746.
- [19] C. Wehrenfennig, M. Liu, H. J. Snaith, M. B. Johnston, L. M. Herz, *Energy Environ. Sci.* **2014**, *7*, 2269.
- [20] S. D. Stranks, G. E. Eperon, G. Grancini, C. Menelaou, M. J. P. Alcocer, T. Leijtens, L. M. Herz, A. Petrozza, H. J. Snaith, *Science* **2013**, *342*, 341.
- [21] G. E. Eperon, S. D. Stranks, C. Menelaou, M. B. Johnston, L. M. Herz, H. J. Snaith, *Energy Environ. Sci.* **2014**, *7*, 982.
- [22] M. Saliba, T. Matsui, J.-Y. Seo, K. Domanski, J.-P. Correa-Baena, M. K. Nazeeruddin, S. M. Zakeeruddin, W. Tress, A. Abate, A. Hagfeldt, M. Grätzel, *Energy Environ. Sci.* **2016**, *9*, 1989.
- [23] E. L. Unger, L. Kegelmann, K. Suchan, D. Sörell, L. Korte, S. Albrecht, *J. Mater. Chem. A* **2017**, *5*, 11401.
- [24] T. Leijtens, K. A. Bush, R. Prasanna, M. D. McGehee, *Nat. Energy* **2018**, *3*, 828.
- [25] I. A. Howard, T. Abzieher, I. M. Hossain, H. Eggers, F. Schackmar, S. Ternes, B. S. Richards, U. Lemmer, U. W. Paetzold, *Adv. Mater.* **2019**, *31*, 1806702.
- [26] W.-Q. Wu, Q. Wang, Y. Fang, Y. Shao, S. Tang, Y. Deng, H. Lu, Y. Liu, T. Li, Z. Yang, A. Gruverman, J. Huang, *Nat. Commun.* **2018**, *9*, 1625.
- [27] Y. Deng, X. Zheng, Y. Bai, Q. Wang, J. Zhao, J. Huang, *Nat. Energy* **2018**, *3*, 560.
- [28] J. B. Whitaker, D. H. Kim, B. W. Larson, F. Zhang, J. J. Berry, M. F. A. M. van Hest, K. Zhu, *Sustainable Energy Fuels* **2018**, *2*, 2442.
- [29] F. Di Giacomo, S. Shanmugam, H. Fledderus, B. J. Bruijnsaers, W. J. H. Verhees, M. S. Dorenkamper, S. C. Veenstra, W. Qiu, R. Gehlhaar, T. Merckx, T. Aernouts, R. Andriessen, Y. Galagan, *Sol. Energy Mater. Sol. Cells* **2018**, *181*, 53.
- [30] Z. Wei, H. Chen, K. Yan, S. Yang, *Angew. Chem., Int. Ed.* **2014**, *53*, 13239.
- [31] S.-G. Li, K.-J. Jiang, M.-J. Su, X.-P. Cui, J.-H. Huang, Q.-Q. Zhang, X.-Q. Zhou, L.-M. Yang, Y.-L. Song, *J. Mater. Chem. A* **2015**, *3*, 9092.
- [32] M. Bag, Z. Jiang, L. A. Renha, S. P. Jeong, V. M. Rotello, D. Venkataraman, *Mater. Lett.* **2016**, *164*, 472.
- [33] F. Mathies, T. Abzieher, A. Hochstuhl, K. Glaser, A. Colmann, U. W. Paetzold, G. Hernandez-Sosa, U. Lemmer, A. Quintilla, *J. Mater. Chem. A* **2016**, *4*, 19207.
- [34] C. Liang, P. Li, H. Gu, Y. Zhang, F. Li, Y. Song, G. Shao, N. Mathews, G. Xing, *Sol. RRL* **2018**, *2*, 1700217.
- [35] P. Li, C. Liang, B. Bao, Y. Li, X. Hu, Y. Wang, Y. Zhang, F. Li, G. Shao, Y. Song, *Nano Energy* **2018**, *46*, 203.
- [36] T. Abzieher, S. Moghadamzadeh, F. Schackmar, H. Eggers, F. Sutterluti, A. Farooq, D. Kojda, K. Habicht, R. Schmager, A. Mertens, R. Azmi, L. Klotz, J. A. Schwenzler, M. Hetterich, U. Lemmer, B. S. Richards, M. Powalla, U. W. Paetzold, *Adv. Energy Mater.* **2019**, *9*, 1802995.
- [37] J. Zimmermann, S. Schliske, M. Held, J.-N. Tisserant, L. Porcarelli, A. Sanchez-Sanchez, D. Mecerreyes, G. Hernandez-Sosa, *Adv. Mater. Technol.* **2019**, *4*, 1800641.
- [38] M. Hösel, R. R. Søndergaard, D. Angmo, F. C. Krebs, *Adv. Eng. Mater.* **2013**, *15*, 995.
- [39] D. Corzo, K. Almasabi, E. Bihar, S. Macphee, D. Rosas-Villalva, N. Gasparini, S. Inal, D. Baran, *Adv. Mater. Technol.* **2019**, *4*, 1900040.
- [40] LG Inkjet-Printed OLED Production Line, <https://www.oled-info.com/lg-display-start-pilot-production-ink-jet-oleds-2017> (accessed: September 2019).
- [41] Kateeva, Kateeva Inkjet Production Line, <http://kateeva.com> (accessed: September 2019).
- [42] S. Schliske, F. Mathies, D. Busko, N. Strobel, T. Rödlmeier, B. S. Richards, U. Lemmer, U. W. Paetzold, G. Hernandez-Sosa, E. Klampaftis, *ACS Appl. Energy Mater.* **2019**, *2*, 764.
- [43] A. Gheno, Y. Huang, J. Bouclé, B. Ratier, A. Rolland, J. Even, S. Vedraine, *Sol. RRL* **2018**, *2*, 1800191.
- [44] L. Zhang, T. Liu, L. Liu, M. Hu, Y. Yang, A. Mei, H. Han, *J. Mater. Chem. A* **2015**, *3*, 9165.
- [45] Hal.archives-ouvertes, Aqueous-Processed Perovskite Solar Cells Based on Reactive Inkjet Printing, <https://hal.archives-ouvertes.fr/hal-01386295/> (accessed: September 2019).
- [46] F. Mathies, H. Eggers, B. S. Richards, G. Hernandez-Sosa, U. Lemmer, U. W. Paetzold, *ACS Appl. Energy Mater.* **2018**, *1*, 1834.
- [47] J. E. Fromm, *IBM J. Res. Dev.* **1984**, *28*, 322.
- [48] P. Calvert, *Chem. Mater.* **2001**, *13*, 3299.
- [49] A. Giuri, E. Saleh, A. Listorti, S. Colella, A. Rizzo, C. Tuck, C. Esposito Corcione, A. Giuri, E. Saleh, A. Listorti, S. Colella, A. Rizzo, C. Tuck, C. Esposito Corcione, *Nanomaterials* **2019**, *9*, 582.
- [50] J. J. van Franeker, K. H. Hendriks, B. J. Bruijnsaers, M. W. G. M. Verhoeven, M. M. Wienk, R. A. J. Janssen, *Adv. Energy Mater.* **2017**, *7*, 1601822.
- [51] Q. Hu, L. Zhao, J. Wu, K. Gao, D. Luo, Y. Jiang, Z. Zhang, C. Zhu, E. Schaible, A. Hexemer, C. Wang, Y. Liu, W. Zhang, M. Grätzel, F. Liu, T. P. Russell, R. Zhu, Q. Gong, *Nat. Commun.* **2017**, *8*, 15688.
- [52] N. J. Jeon, J. H. Noh, Y. C. Kim, W. S. Yang, S. Ryu, S. Il Seok, *Nat. Mater.* **2014**, *13*, 897.
- [53] X. Li, D. Bi, C. Yi, J.-D. Décoppet, J. Luo, S. M. Zakeeruddin, A. Hagfeldt, M. Grätzel, *Science* **2016**, *353*, 58.
- [54] W. Zhang, M. Anaya, G. Lozano, M. E. Calvo, M. B. Johnston, H. Míguez, H. J. Snaith, *Nano Lett.* **2015**, *15*, 1698.
- [55] S. G. Hashmi, D. Martineau, X. Li, M. Ozkan, A. Tiihonen, M. I. Dar, T. Sarikka, S. M. Zakeeruddin, J. Paltakari, P. D. Lund, M. Grätzel, *Adv. Mater. Technol.* **2017**, *2*, 1600183.
- [56] Y. Wang, J. Wu, P. Zhang, D. Liu, T. Zhang, L. Ji, X. Gu, Z. David Chen, S. Li, *Nano Energy* **2017**, *39*, 616.
- [57] D. K. Owens, R. C. Wendt, *J. Appl. Polym. Sci.* **1969**, *13*, 1741.
- [58] W. Rabel, *Farbe Lack* **1971**, *10*, S997.
- [59] D. H. Kaelble, *J. Adhes.* **1970**, *2*, 66.
- [60] Y. Deng, X. Zheng, Y. Bai, Q. Wang, J. Zhao, J. Huang, *Nat. Energy* **2018**, *3*, 560.
- [61] J. B. Whitaker, D. H. Kim, B. W. Larson, F. Zhang, J. J. Berry, M. F. A. M. van Hest, K. Zhu, *Sustainable Energy Fuels* **2018**, *2*, 2442.
- [62] T. Abzieher, J. A. Schwenzler, S. Moghadamzadeh, F. Sutterluti, I. M. Hossain, M. Pfau, E. Lotter, M. Hetterich, B. S. Richards, U. Lemmer, M. Powalla, U. W. Paetzold, *IEEE J. Photovoltaics* **2019**, *9*, 1249.
- [63] T. J. Jacobsson, L. J. Schwan, M. Ottosson, A. Hagfeldt, T. Edvinsson, *Inorg. Chem.* **2015**, *54*, 10678.
- [64] P. Fassl, V. Lami, A. Bausch, Z. Wang, M. T. Klug, H. J. Snaith, Y. Vaynzof, *Energy Environ. Sci.* **2018**, *11*, 3380.
- [65] T. J. Jacobsson, J.-P. Correa-Baena, E. Halvani Anaraki, B. Philippe, S. D. Stranks, M. E. F. Bouduban, W. Tress, K. Schenk, J. Teuscher, J.-E. Moser, H. Rensmo, A. Hagfeldt, *J. Am. Chem. Soc.* **2016**, *138*, 10331.

- [66] B. Philippe, M. Saliba, J.-P. Correa-Baena, U. B. Cappel, S.-H. Turren-Cruz, M. Grätzel, A. Hagfeldt, H. Rensmo, *Chem. Mater.* **2017**, *29*, 3589.
- [67] Q. Sun, P. Fassel, Y. Vaynzof, *ACS Appl. Energy Mater.* **2018**, *1*, 2410.
- [68] K. X. Steirer, P. Schulz, G. Teeter, V. Stevanovic, M. Yang, K. Zhu, J. J. Berry, *ACS Energy Lett.* **2016**, *1*, 360.
- [69] P.-W. Liang, C.-Y. Liao, C.-C. Chueh, F. Zuo, S. T. Williams, X.-K. Xin, J. Lin, A. K.-Y. Jen, *Adv. Mater.* **2014**, *26*, 3748.
- [70] Q. Chen, H. Zhou, T.-B. Song, S. Luo, Z. Hong, H.-S. Duan, L. Dou, Y. Liu, Y. Yang, *Nano Lett.* **2014**, *14*, 4158.
- [71] L. Wang, C. McCleese, A. Kovalsky, Y. Zhao, C. Burda, *J. Am. Chem. Soc.* **2014**, *136*, 12205.
- [72] S. Liu, W. Huang, P. Liao, N. Pootrakulchote, H. Li, J. Lu, J. Li, F. Huang, X. Shai, X. Zhao, Y. Shen, Y.-B. Cheng, M. Wang, *J. Mater. Chem. A* **2017**, *5*, 22952.
- [73] M. Stolterfoht, C. M. Wolff, Y. Amir, A. Paulke, L. Perdigón-Toro, P. Caprioglio, D. Neher, *Energy Environ. Sci.* **2017**, *10*, 1530.
- [74] W. E. I. Sha, X. Ren, L. Chen, W. C. H. Choy, *Appl. Phys. Lett.* **2015**, *106*, 221104.
- [75] A. A. B. Baloch, M. I. Hossain, N. Tabet, F. H. Alharbi, *J. Phys. Chem. Lett.* **2018**, *9*, 426.